Elastic guided waves in helical multi-wire armors

Fabien Treyssède, Laurent Laguerre, Patrice Cartraud, T. Soulard

Version of Record: https://www.sciencedirect.com/science/article/pii/S0041624X20302328
Manuscript_5ac2ef75cc1525a4fd7025c285627689

Elastic guided waves in helical multi-wire armors

F. Treyssède[a,*], L. Laguerre[a], P. Cartraud[b], T. Soulard[c]

[a] *GERS-GeoEND, Univ Gustave Eiffel, IFSTTAR, F-44344 Bouguenais, France*
[b] *GeM, UMR CNRS 6183, Centrale Nantes, F-44321 Nantes, France*
[c] *LHEAA, UMR CNRS 6598, Centrale Nantes, F-44321 Nantes, France*

Abstract

In this paper, a numerical method is proposed to investigate the propagation of elastic guided waves in the armors protecting cylindrical structures, such as cables and pipes, and evaluate the feasibility of using these waves in the context of non-destructive evaluation and structural health monitoring. Armors usually consist of a large number of helical wires in contact with polymeric sheaths surrounding the structure. The numerical method combines a semi-analytical finite element method written in twisting coordinates, which accounts for the continuous screw symmetry of the problem along the structure axis, with rotational Bloch conditions in the cross-section in order to account for the high order of the discrete circular symmetry. The proposed formulation allows the initial three-dimensional problem to be reduced to a two-dimensional unit cell involving only one wire, well suited for fast computations of contact problems and dispersion curves. The existence of wave modes along the two directions (screw axis and circumferential direction) is justified from a theoretical point of view by considering the metric tensor of a mixed twisting-polar coordinate system. Numerical results are presented for a typical armor of power cable, focusing on longitudinal waves propagating predominantly inside the wires. The internal part of the cable is approximated as a homogenized medium to preserve the continuous screw symmetry of the problem. A comparison with experimental measurements is carried out. The results show that the modal velocity of longitudinal waves behaves as in a single free wire above a limit frequency identified by the model. This is not the case of modal attenuation, always greater in the armor due to mechanical contact with the viscoelastic sheaths. Two modes of potential interest for the non-destructive evaluation of armors are identified. The influence of mechanical contacts on wave propagation in armors is finally discussed, including interwire contact.

Keywords: waveguide, helical, rotational symmetry, finite element, cable, wire

1. Introduction

Elastic guided waves are of potential interest for the non-destructive evaluation (NDE) and the structural health monitoring (SHM) of elongated structures [1]. Compared to bulk waves, guided waves can propagate over longer distances. These waves are typically excited in a high-frequency regime (ultrasonic) allowing relatively small defects to be detected. It is of interest to evaluate the feasibility of using guided waves for the NDE of the armors protecting cylindrical structures such as cables and pipes. Armors are multi-wired and often consist of one or two cylindrical layers of helical wires surrounding the structure. Their essential function is to mechanically reinforce the structure, typically against bending fatigue and extreme conditions, or during installation. Armors are widely encountered in offshore applications to protect submarine power cables (in the energy industry) and flexible pipes (in the oil and gas industry) – see *e.g.* Refs. [2, 3].

The propagation of guided waves is complex in nature. Such waves are dispersive and multimodal. In practice, modeling tools are required to understand the mechanisms of their propagation, interpret experimental measurements at a laboratory scale, and optimize inspection techniques for real-field applications [1]. Typically, the knowledge of

*Corresponding author
Email address: fabien.treyssede@ifsttar.fr (F. Treyssède)

dispersion curves of wave velocities and attenuations as functions of frequency help to maximize the propagation distance of wave modes in a frequency range of interest (among other factors).

The propagation of waves in multi-wire structures has already been investigated, both experimentally and numerically, considering seven-wire strands (see *e.g.* Refs. [4, 5, 6, 7, 8, 9, 10, 11, 12, 13]), aluminum conductor steel reinforced cables [14, 15, 16, 17] or steel multi-wire ropes [18, 19]. Up to the authors knowledge, cable armors have not yet been considered in the literature. Furthermore, the modeling approaches used in these studies are generally based on fully three-dimensional transient finite element simulations, or geometrical simplifications neglecting curvature and contact phenomena, which does not allow a full and accurate determination of dispersion curves.

The modeling of wave propagation in armors faces several difficulties: helical geometry (screw symmetry), prestress effect, mechanical contact (wires are coupled to polymeric sheaths), a large number of wires... Part of these difficulties have already been addressed, in the modeling of seven-wire strands [20, 21, 22, 23], thanks to a semi-analytical finite element (SAFE) method expressed in a twisting coordinate system. This method exploits the continuous screw symmetry of the problem by adopting an analytical description along the screw axis while discretizing the transverse coordinates (cross-section). The initial three-dimensional (3D) problem is hence reduced to a two-dimensional (2D) model.

Note that the SAFE approach has been extensively used for the computation of modes in 3D translationally symmetric waveguides (see *e.g.* Refs. [24, 25, 26]). Alternatively, the so-called wave finite element (WFE) method (see *e.g.* Refs. [27, 28]), which consists in applying periodic boundary conditions to a single repetitive unit cell, could also be used. Its computational cost is yet greater than with the SAFE method (the WFE unit cell is 3D). Because the problem considered in the present paper involves a relatively large amount of degrees of freedom, the SAFE approach is preferred.

However, this model reduction is insufficient for armors. Compared to seven-wire strands, armors are highly multi-wired (the number of wires is large and usually exceeds fifty). Fortunately, the problem can be further reduced by taking advantage of another symmetry: the discrete rotational symmetry (circular periodicity) of the cross-section. This type of reduction has been recently validated with seven-wire strands [29].

The goal of this paper is twofold. First, the above-mentioned modeling principles are specifically applied to helical armors involving a large number of wires. The order of the rotational symmetry is equal to the number of wires, which will be denoted as N in this paper. The initial 3D problem is hence reduced to a 2D/N model, as depicted by the example in Fig. 1. This reduction yields fast computations, well-suited for contact problems, the analysis of wave modes and the determination of dispersion curves. The numerical approach applies to any wire cross-section shape: circular, flat, etc. Second, the feasibility of using guided waves for the NDE of armors consisting of circular wires is evaluated thanks to numerical simulations as well as comparison with experiments. Our study mainly focuses on a relatively high-frequency regime, that is to say, such that the bulk wavelengths are at most of the order of the diameter of wires (the wavelengths hence remain significantly lower than the diameter of the overall structure protected by the armor).

This paper is organized as follows. Section 2 recalls the SAFE approach in twisting coordinates and details how to account for the rotational symmetry of the cross-section. In particular, the existence of wave modes along the two directions (screw axis and circumferential direction) is justified from a theoretical point of view. Section 3 presents some numerical results for a typical armor of power cable. The analysis focuses on waves propagating predominantly inside the wires. A comparison with experimental measurements is finally carried out.

The internal part of power cables is often constituted by helical conductors having a torsion different from the armor itself, so that the screw symmetry of the whole structure may be broken. To circumvent this problem, the internal part will be approximated as a homogenized medium in this paper. This approximation is justified by our interest in the NDE of armor, excluding the internal part (the frequency regime of waves is supposed to be high enough to avoid significant interactions with the core).

Armors may involve one or several layers of wires. The numerical approach proposed in this paper is restricted to continuous screw symmetric armors and hence remains applicable as long as the layers are twisted with the same rate. In the case of double-layer armors, the two protecting layers of wires can be twisted in opposite directions, which breaks the continuous symmetry of the problem and hereby excludes the use of the SAFE approach.

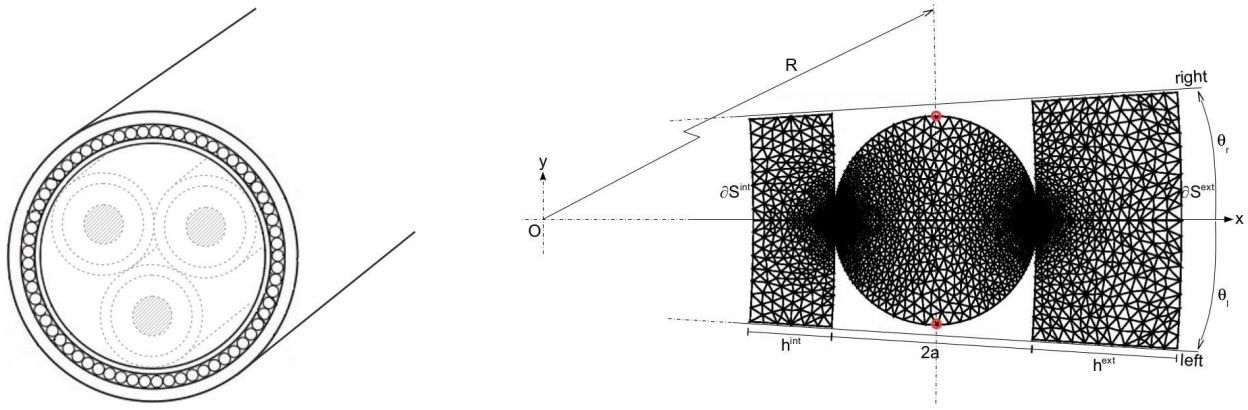

(a) (b)

Figure 1: (a) Example of armor of power cables: the structure typically consists of helical steel wires surrounded by polymeric inner and outer sheaths, and protects the active part including electrical conductors (sketched with dashed gray lines). (b) Reduction from a 3D problem to a 2D/N model by accounting for the continuous screw symmetry as well as for the discrete rotational symmetry of the cross-section (the resulting 2D unit cell is delimited by left and right boundaries linked together with circular periodic conditions). The two red circles indicate the pair of nodes used in Sec. 4.3 to artificially enforce interwire contact.

2. Numerical method

2.1. Background: screw symmetric formulation (2D model)

This section briefly recalls the numerical method accounting for the continuous screw symmetry, hence allowing the initial 3D problem to be reduced to a 2D model. A time-harmonic dependence in $e^{-i\omega t}$ is adopted.

2.1.1. SAFE approach

The analysis of guided waves inside multi-wire helical structures requires a specific curvilinear coordinate system, called twisting coordinate system. Such a system has constant non zero torsion but zero curvature. The torsion of the twisting system is defined by $\tau_0 = 2\pi/L_0$, with L_0 denoting the helix pitch of wires under prestress. With this kind of system, the cross-section plane remains perpendicular to the straight axis but rotates around this axis by following the helical wires. This subsection briefly reviews the main equations of the SAFE method written in a twisting system and including prestress effects. Further details can be found in Refs. [21, 22, 23].

Let us denote z the straight axis of the waveguide, fixed to the Cartesian system, (x, y) the cross-section twisting coordinates, k the axial wavenumber and ω the angular frequency. The application of a SAFE method consists in assuming an $e^{i(kz-\omega t)}$ dependence of acoustic fields before finite element (FE) discretization. Therefore, only the 2D cross-section in the (x, y) plane of the structure needs to be meshed.

The application of a SAFE method to the equilibrium equations of elastodynamics leads to the following matrix system:

$$\{\mathbf{K}_{1\sigma} - \omega^2\mathbf{M} + ik(\mathbf{K}_{2\sigma} - \mathbf{K}_{2\sigma}^{\mathrm{T}}) + k^2\mathbf{K}_{3\sigma}\}\mathbf{U} = \mathbf{F}, \tag{1}$$

where $\mathbf{U}$ is the vector of nodal displacements, with three degrees of freedom per node, expressed in the orthonormal Serret-Frenet basis $(\mathbf{e}_x, \mathbf{e}_y, \mathbf{e}_z)$ associated with the twisting system. The expressions of matrices, which involve operators depending on the torsion τ_0, can be found in Ref. [23]. The index σ highlights the dependence of SAFE matrices on the Cauchy prestress tensor $\boldsymbol{\sigma}_0$, where the subscript 0 refers to the prestress configuration. The right-hand side $\mathbf{F}$ is the force vector. Equation (1) can be viewed as the so-called linearized updated Lagrangian formulation of nonlinear mechanics (see e.g. [30] for instance), here further transformed into a SAFE formulation expressed in twisting coordinates. The FE mesh used to calculate the matrices corresponds to the prestressed cross-section S_0, statically deformed under prestress and obtained from the updating of the initial FE mesh.

2.1.2. Prestress state

The first step of the analysis consists in computing the static prestress state. This state is loaded by a constant tensile strain ϵ_0. Similarly to a SAFE method, its computation can be achieved efficiently from a 2D cross-section model, using a homogenization method specifically written in twisting coordinates. Theoretical details can be found in Ref. [21]. Such a method leads to a linear system, reduced on the cross-section, of the form:

$$\mathbf{K}_0\mathbf{U}_0 = \mathbf{F}_0 + \mathbf{F}'_0 \tag{2}$$

where $\mathbf{U}_0$ is the static nodal displacement vector (microscopic) and $\mathbf{F}_0$ is the external load vector depending on the prescribed axial strain ϵ_0 (macroscopic). Note that $\mathbf{K}_0$ and $\mathbf{F}_0$ are integrated on the initial cross-section S (undeformed) and depend on the initial torsion τ of the undeformed geometry. The torsion τ_0 of the deformed geometry is related to τ by: $\tau_0 = \tau/(1+\epsilon_0)$. The expressions of $\mathbf{K}_0$ and $\mathbf{F}_0$ can be found in Ref. [23] and are not repeated here for paper conciseness.

The second term in the right hand side of Eq. (2) is specific to the present paper and corresponds to the load vector relative to the pressure p_0 of the fluid, which typically acts on the outer sheath of armors. The element vector corresponding to this term is given by:

$$\mathbf{F}'^e_0 = -\int_{\partial S^e} \mathbf{N}^{eT} p_0 \mathbf{n} \mathrm{d}\partial S \tag{3}$$

where ∂S denotes the contour of the initial cross-section S, $\mathbf{n}$ is its unit outward normal and $\mathbf{N}^e(u)$ is the matrix of one-dimensional functions used to interpolate the displacement vector along the curve (u has to be understood as the local coordinate along the one-dimensional element). For a given element, the position vector of a point M on the pressurized surface is parametrized by:

$$\mathbf{OM}(u,z) = x(u)\mathbf{e}_x(z) + y(u)\mathbf{e}_y(z) + z\mathbf{e}_z \tag{4}$$

The normal involved in Eq. (3) can then be obtained from the relation:

$$\mathbf{n}\mathrm{d}\partial S\,\mathrm{d}z = \frac{\partial \mathbf{OM}}{\partial u} \times \frac{\partial \mathbf{OM}}{\partial z}\mathrm{d}u\mathrm{d}z \tag{5}$$

The first term of the cross-product, $\partial\mathbf{OM}/\partial u$, is approximated thanks to the one-dimensional FE interpolation of the curve ∂S. From Eq. (4) and the Serret-Frenet relations in the twisting system, $\partial\mathbf{e}_x/\partial z = \tau\mathbf{e}_y$, $\partial\mathbf{e}_y/\partial z = -\tau\mathbf{e}_x$ (see Ref. [21]), the calculation of the second term leads to: $\partial\mathbf{OM}/\partial z = -\tau y\mathbf{e}_x + \tau x\mathbf{e}_y + \mathbf{e}_z$. The element vector given by Eq. (3) can then be readily computed.

Finally, the Cauchy prestress $\boldsymbol{\sigma}_0$, necessary for the calculation of the SAFE matrices involved in Eq. (1), can be post-processed from the solution of Eq. (2).

It has to be emphasized that the external pressure increases the contact width between the sheaths and the wires. Besides, the tensile strain tends to increase the contact width with the inner sheath because of the helical geometry of wires (yielding a radial compression of the core). These contact phenomena are neglected when the linear static problem given by Eq. (2) is solved in a unique step. Instead, an iterative procedure must be used in order to account for the contact evolution (non-linear by nature). Our modeling approach is based on a node-to-node contact procedure using a direct elimination method [31]. A matching mesh is used inside the interfacial zone. For the 2D cross-section FE model used in this paper, the computation starts with a single point contact. As the external load is incremented, contact pairs of nodes are successively formed: once the gap between a pair of nodes is closed, the continuity of displacement is enforced at these nodes by the direct elimination method. The continuity is enforced along the three directions, hence corresponding to the assumption of stick contact conditions (infinite friction). The reader may refer to [23] for additional details on this iterative procedure.

2.2. Introducing discrete rotational symmetry (2D/N model)

In this paper, the SAFE approach, which accounts for continuous screw symmetry, is combined with circular Bloch conditions to consider discrete rotational symmetry. This enables to reduce the computational domain to a unit cell.

The unit cell of the cross-section is delimited by left and right boundaries as shown in Fig. 1b. The displacement and force vectors are partitioned as follows: $\mathbf{U} = [\mathbf{U}_l^{\mathrm{T}}\ \mathbf{U}_i^{\mathrm{T}}\ \mathbf{U}_r^{\mathrm{T}}]^{\mathrm{T}}$, $\mathbf{F} = [\mathbf{F}_l^{\mathrm{T}}\ \mathbf{F}_i^{\mathrm{T}}\ \mathbf{F}_r^{\mathrm{T}}]^{\mathrm{T}}$, where the subscripts l and r are used to denote the degrees of freedom (dofs) of the left and right boundaries respectively. The subscript i denotes the internal dofs.

The left and right dofs are linked together thanks to boundary conditions of Bloch type (see e.g. [32, 33]). Let us recall the Bloch conditions in the usual case of a scalar wave field ϕ, and its dual variable ψ, when the periodicity occurs in a straight direction. These conditions are: $\phi_r = \lambda\phi_l$ and $\psi_r = -\lambda\psi_l$, where $\lambda = \mathrm{e}^{\mathrm{i}\mu}$ ($\mathrm{i}\mu$ is often called the propagation constant).

However, the periodicity of interest in this paper is of rotational type and involves non-scalar wavefields (the displacement and force vectors). The Bloch conditions have to be expressed along a circumferential direction in an appropriate frame, corresponding to a coordinate system of polar type. Since the displacement components $\mathbf{U}_l$ and $\mathbf{U}_r$ are initially expressed in the (x, y, z) twisting frame, they must be transformed to a mixed twisting-polar frame. This frame will be denoted as (ρ, θ, z). The polar coordinates are defined from the twisting coordinates in the cross-section through he relation $(x, y) = (\rho\cos\theta, \rho\sin\theta)$.

Let us denote $\mathbf{Q}_l$ and $\mathbf{Q}_r$ the transformation matrices of $\mathbf{U}_l$ and $\mathbf{U}_r$ from the twisting frame to the mixed twisting-polar frame. The rotational periodic conditions for the displacement and force vector fields are then expressed as:

$$\mathbf{Q}_r\mathbf{U}_r = \lambda\mathbf{Q}_l\mathbf{U}_l \tag{6a}$$

$$\mathbf{Q}_r\mathbf{F}_r = -\lambda\mathbf{Q}_l\mathbf{F}_l \tag{6b}$$

where $\mathbf{Q}_{l,r}$ are block diagonal transformation matrices consisting of three-by-three sub-matrices for the three displacement components at every node. These sub-matrices, denoted as $\mathbf{q}_{l,r}$, are given by:

$$\mathbf{q}_{l,r} = \begin{bmatrix} \cos\theta_{l,r} & \sin\theta_{l,r} & 0 \\ -\sin\theta_{l,r} & \cos\theta_{l,r} & 0 \\ 0 & 0 & 1 \end{bmatrix} \tag{7}$$

where θ_l and θ_r are the angles of the left and right boundaries respectively (see Fig. 1b). The matrices $\mathbf{q}_{l,r}$ are orthogonal so that $\mathbf{Q}_{l,r}^{-1} = \mathbf{Q}_{l,r}^{\mathrm{T}}$.

Because the structure is divided into N rotationally periodic cells, any wavefield at the right boundary of the Nth cell must be equal to the field at the left boundary of the first cell, so that $\lambda^N = 1$. Therefore, the propagation factor can be written as:

$$\lambda(n) = \mathrm{e}^{\mathrm{i}2n\pi/N} \tag{8}$$

where n is a user-defined integer lying inside a set of N consecutive integers. In this paper, the following numbering is adopted:

$$n = \begin{cases} -\frac{N}{2}+1, ..., 0, ..., \frac{N}{2} & \text{for } N \text{ even} \\ -\frac{N-1}{2}, ..., 0, ..., \frac{N-1}{2} & \text{for } N \text{ odd} \end{cases} \tag{9}$$

in order to pair right-handed modes ($n > 0$, rotating anti-clockwise around the z-axis) with left-handed modes ($n < 0$, rotating clockwise) [29]. The modes $n = 0$ are rotationally symmmetric.

From Eq. (6a) written for a given n, the displacement vector $\mathbf{U}$ can be reduced to:

$$\mathbf{U} = \mathbf{R}(n)\tilde{\mathbf{U}}, \quad \mathbf{R}(n) = \begin{bmatrix} \mathbf{I} & \mathbf{0} \\ \mathbf{0} & \mathbf{I} \\ \lambda(n)\mathbf{Q}_r^{-1}\mathbf{Q}_l & \mathbf{0} \end{bmatrix}, \quad \tilde{\mathbf{U}} = \begin{bmatrix} \mathbf{U}_l \\ \mathbf{U}_i \end{bmatrix}. \tag{10}$$

Based on the reduced displacement vector $\tilde{\mathbf{U}}$, Eq. (1) can then be rewritten as:

$$\left\{\tilde{\mathbf{K}}_{1\sigma}(n) - \omega^2\tilde{\mathbf{M}}(n) + \mathrm{i}k\left(\tilde{\mathbf{K}}_{2\sigma}(n) - \tilde{\mathbf{K}}_{2\sigma}(-n)^{\mathrm{T}}\right) + k^2\tilde{\mathbf{K}}_{3\sigma}(n)\right\}\tilde{\mathbf{U}} = \mathbf{0} \tag{11}$$

where $\tilde{\mathbf{K}}_{i\sigma}(n) = \mathbf{R}(n)^{\mathrm{H}}\mathbf{K}_{i\sigma}\mathbf{R}(n)$ ($i = 1, 2, 3$) and $\tilde{\mathbf{M}}(n) = \mathbf{R}(n)^{\mathrm{H}}\mathbf{M}\mathbf{R}(n)$. The superscript H denotes complex conjugate transpose.

In Eq. (11), the right hand side actually stems from the term $\mathbf{R}(n)^{\mathrm{H}}\mathbf{F}$, which vanishes as shown hereafter. Our attention is restricted to the free response in the purpose of computing eigenmodes. Hence, there are no forces acting on internal dofs because acoustic sources are discarded ($\mathbf{F}_i = \mathbf{0}$). Accounting for the orthogonality of $\mathbf{Q}_{l,r}$, the expansion of $\mathbf{R}(n)^{\mathrm{H}}\mathbf{F}$ leads to:

$$\mathbf{R}(n)^{\mathrm{H}}\mathbf{F} = \begin{bmatrix} \mathbf{F}_l + \overline{\lambda}\mathbf{Q}_l^{-1}\mathbf{Q}_r\mathbf{F}_r \\ \mathbf{0} \end{bmatrix} \tag{12}$$

where the overbar denotes complex conjugate. Equation (6b) leads to $\mathbf{F}_l + \overline{\lambda}\mathbf{Q}_l^{-1}\mathbf{Q}_r\mathbf{F}_r = (1 - |\lambda|^2)\mathbf{F}_l$, which vanishes because $|\lambda| = 1$ from Eq. (8).

Equation (11) is therefore a homogeneous equation, corresponding to the eigensystem that accounts both for the continuous helical symmetry (using the SAFE approach) and for the discrete rotational symmetry of the cross-section (thanks to the application of Bloch conditions). Throughout this paper, the mth eigensolution obtained for a given circumferential order n will be denoted as follows:

$$\{k_m^{(n)}, \tilde{\mathbf{U}}_m^{(n)}\} \tag{13}$$

The modal excitability, which will be a quantity of interest in this paper, is now introduced. For a given frequency, the excitability of a particular mode can be defined as the ratio of the displacement of that mode to a point force applied in a given direction. In this paper, the excitability can be obtained in a straightforward manner by noticing that the matrices involved in Eq. (11) have the same symmetry properties than those used to derive the excitability in Ref. [29]. The excitability matrix, denoted as $\mathbf{E}_m^{(n)}$, can then be written as:

$$\mathbf{E}_m^{(n)} = \frac{\mathrm{i}\omega}{4Q_{m,-m}^{(n,-n)}} \tilde{\mathbf{U}}_m^{(n)} \tilde{\mathbf{U}}_{-m}^{(-n)\mathrm{T}} \tag{14}$$

where $\tilde{\mathbf{U}}_{-m}^{(-n)}$ denotes the mode paired with $\tilde{\mathbf{U}}_m^{(n)}$, traveling in the opposite directions both axially and circumferentially, and the normalization factor $Q_{m,-m}^{(n,-n)}$ is given by:

$$Q_{m,-m}^{(n,-n)} = \mathrm{i}\frac{\omega}{4}\left(\tilde{\mathbf{T}}_{-m}^{(-n)\mathrm{T}} \tilde{\mathbf{U}}_m^{(n)} - \tilde{\mathbf{U}}_{-m}^{(-n)\mathrm{T}} \tilde{\mathbf{T}}_m^{(n)}\right) \tag{15}$$

with $\tilde{\mathbf{T}}_m^{(n)} = \left(\tilde{\mathbf{K}}_2(-n)^{\mathrm{T}} + ik_m^{(n)}\tilde{\mathbf{K}}_3(n)\right)\tilde{\mathbf{U}}_m^{(n)}$. The vector $\tilde{\mathbf{T}}_m^{(n)}$ can be interpreted as the modal force associated with the eigendisplacement $\tilde{\mathbf{U}}_m^{(n)}$. In Eq. (14), the matrix element $\left(\mathbf{E}_m^{(n)}\right)_{ij}$ represents the displacement amplitude of the mth wavemode of circumferential order n at dof i when a unit point force acts at dof j.

Finally, as far as the prestress state is concerned, one assumes rotationally symmetric loads ($n = 0$) so that, following the same approach as previously, the static problem reduces to:

$$\tilde{\mathbf{K}}_0\tilde{\mathbf{U}}_0 = \mathbf{R}(0)^{\mathrm{H}}(\mathbf{F}_0 + \mathbf{F}_0') \tag{16}$$

with $\tilde{\mathbf{K}}_0 = \mathbf{R}(0)^{\mathrm{H}}\mathbf{K}_0\mathbf{R}(0)$ and $\tilde{\mathbf{U}}_0 = [\mathbf{U}_{0_l}^{\mathrm{T}}\ \mathbf{U}_{0_i}^{\mathrm{T}}]^{\mathrm{T}}$.

2.3. Justification of the existence of wave modes

The $\mathrm{e}^{\mathrm{i}kz}$ dependence assumed for wave fields in Sec. 2.1.1 implies that axial variables must be separable from transverse variables in the governing equations of motion. As justified in Refs. [20, 34], this separation of variables is possible thanks to the independence of the metric tensor of the twisting system on the z coordinate. Note that the prestressed state must not vary along the z-axis, otherwise the separation of the z-variable would not be possible. In practice, this condition is fulfilled, at least far enough from the ends where the axial loads are applied, so that the prestressed state can be considered as invariant along z. This justifies the existence of wave modes in the axial direction of helical structures. However, the question of existence of Bloch waves in the circumferential direction of a twisting system has not been considered.

Starting from the helical coordinate system defined in Ref. [20] but using the polar coordinates (ρ, θ) instead of the rectangular cross-section coordinates yields the following expression for the position vector of any point M in the 3D space:

$$\mathbf{OM}(\rho, \theta, s) = \mathbf{r}(s) + \rho\cos\theta\mathbf{e}_n(s) + \rho\sin\theta\mathbf{e}_b(s) \tag{17}$$

Number of wires N	Torsion τa	Helix radius of wires R/a	Thickness of outer sheath h^{ext}/a	Thickness of inner sheath h^{int}/a
50	0.121e-01	17.578	1.422	0.800

Table 1: Dimensionless geometrical parameters. The helix lay angle $\phi = \tan^{-1}(R\tau)$ is equal to 12°. The parameters are given in the initial state (undeformed, unprestressed).

	Density ρ (kg/m^3)	Longitudinal velocity c_l (m/s)	Shear velocity c_s (m/s)	Longitudinal bulk wave attenuation κ_l (Np/λ)	Shear bulk wave attenuation κ_s (Np/λ)
steel	7800	6091.4	3256.0	0.003	0.008
PE	1000	1198.2	489.2	0.02	0.16

Table 2: Material properties.

Based on Serret-Frenet formula, the calculation of the covariant basis $(\partial\mathbf{OM}/\partial\rho, \partial\mathbf{OM}/\partial\theta, \partial\mathbf{OM}/\partial s)$, denoted by $(\mathbf{g}_1, \mathbf{g}_2, \mathbf{g}_3)$, gives:

$$\begin{aligned} \mathbf{g}_1 &= \cos\theta\mathbf{e}_n(s) + \sin\theta\mathbf{e}_b(s),\ \mathbf{g}_2 = -\rho\sin\theta\mathbf{e}_n(s) + \rho\cos\theta\mathbf{e}_b(s), \\ \mathbf{g}_3 &= -\tau\rho\sin\theta\mathbf{e}_n(s) + \tau\rho\cos\theta\mathbf{e}_b(s) + (1+\kappa\rho\cos\theta)\mathbf{e}_t(s) \end{aligned} \tag{18}$$

so that the metric tensor, defined by $(\mathbf{g})_{ij} = \mathbf{g}_i \cdot \mathbf{g}_j$, is:

$$\mathbf{g} = \begin{bmatrix} 1 & 0 & 0 \\ 0 & \rho^2 & \tau\rho^2 \\ 0 & \tau\rho^2 & \tau^2\rho^2 + (1+\kappa\rho\cos\theta)^2 \end{bmatrix}. \tag{19}$$

In Eqs. (17)–(19), s denotes the helical coordinate, $\mathbf{r}(s)$ is the position vector on the helix centreline, $(\mathbf{e}_n, \mathbf{e}_b, \mathbf{e}_t)$ is the Serret-Frenet basis associated with the helix, κ and τ are the helix curvature and torsion respectively.

The metric tensor given by Eq. (19) is for a helical-polar coordinate system and depends on θ. Yet, the coordinate system of interest in this paper is a twisting system, which can be viewed as a particular case of helical system having no curvature ($\kappa = 0$, $s = z$, $\mathbf{r}(z) = z\mathbf{e}_z$). Therefore, the dependence on θ disappears in Eq. (19): the metric tensor of a mixed twisting-polar system only depends on the radial coordinate ρ. As a consequence, the coefficients of any partial differential operators expressed in the so-defined coordinate system are independent of θ and z, which justifies the simultaneous existence of wave modes in the axial and the circumferential directions.

Based on the SAFE formulation written in twisting coordinates (Sec. 2.1.1), there is no need to rewrite the equilibrium equations in the polar frame to account for rotational symmetry because the circular periodicity of the problem is applied through boundary conditions. These periodic conditions yet involve vector fields, which must be expressed with polar components, as done in Sec. 2.2 through Eq. (6).

3. Results

In this section, the propagation of guided waves is investigated inside the armor of a power cable. The armor consists of metallic helical wires of circular cross-section in mechanical contact with polymeric sheaths.

3.1. Model description

The geometrical parameters of the armor, represented in Fig. 1b, are summarized in Table 1. The wire radius, denoted as a, is used as the characteristic length to normalize the geometrical parameters. The dimensionless radius of the whole cross-section is hence given by $(R + a + h^{\text{ext}})/a = 20$. The wires and sheaths are made of steel and polyethylene (PE) material respectively. The material properties are listed in Table 2. Viscoelastic losses are taken into account in the model in order to evaluate the propagation distance of guided waves. The bulk wave attenuations given in Table 2 have been estimated from Refs. [35, 36].

The cross-section of the armor has been meshed with Gmsh [37]. Figure 1b depicts the FE mesh of the unit cell, reduced to a single wire in contact with the inner and the outer sheaths. There is no contact between adjacent wires. This assumption will be discussed in Sec. 4. The mesh is refined near contact regions with a specified number of elements to properly discretize the contact width. Six-node triangles have been used (quadratic triangular elements), yielding 28,413 degrees of freedom. The element length satisfies a meshing criterion of at least 5 elements per steel wavelength (the minimum wavelength in steel is its shear wavelength at the maximum frequency), that is to say, roughly 10 nodes per steel wavelength owing to the quadratic interpolation.

As outlined in Sec. 2, the computations are performed in two steps. In the first step, the static state of the structure (prestressed state) is computed. The prestress tensor, necessary for the calculation of the SAFE matrices, is post-processed and the FE mesh of the cross-section is updated. In its prestressed state, the cable is statically loaded by an external pressure $p_0 = 20$ bars and a tensile strain $\epsilon_0 = 0.1\%$. The numerical results obtained for the static prestress state are briefly presented in Sec. 3.2.

In the second step, the dynamic problem given by Eq. (11) is solved. The ARPACK library [38] is used. This library is appropriate for large sparse matrices and based on the implicitly restarted Arnoldi method. The calculations are performed for 200 frequencies uniformly distributed in the interval $[0, 5]$MHz-mm. With the ARPACK library, a specified number of eigenvalues k can be looked for around a user-defined shift k_0. In order to avoid the computations of too many modes resonating predominantly inside the PE sheaths, a specified number of 20 eigenvalues is looked for around the longitudinal bulk wavenumber of steel $k_0 = \omega/c_l$. The longitudinal wave modes of wires, which will be denoted as L(0,n), are expected to occur close to this value.

Note that the internal part of the cable is not discretized because we are interested in waves propagating predominantly inside the wires, *i.e.* waves that are weakly affected by the media outside the armor. Besides, the internal part is often constituted by helical conductors having a torsion different from the armor itself, so that the screw symmetry of the complete structure may be broken. Instead, the internal part is approximated as a homogenized cylindrical medium with Poisson ratio ν_h. This approximation leads to the following static boundary condition applied on the internal boundary S^{int} of the inner sheath for the prestress state:

$$\mathbf{u}_0 \cdot \mathbf{n} = -\nu_h R^{\text{int}} \epsilon_0 \qquad \text{on } S^{\text{int}} \tag{20}$$

where $R^{\text{int}} = R - a - h^{\text{int}}$ denotes the internal radius of the inner sheath. The above condition enforces the radial displacement generated by the Poisson effect due to the applied axial strain ϵ_0. For the numerical results of this paper, the value of $\nu_h = 0.3$ has been set. Additionally, a free static boundary condition is applied on the external surface S^{ext} of the outer sheath:

$$\boldsymbol{\sigma}_0 \cdot \mathbf{n} = -p_0 \mathbf{n} \qquad \text{on } S^{\text{ext}} \tag{21}$$

As far as wave perturbations are concerned, the dynamic boundary conditions chosen are stress-free on both surfaces:

$$\boldsymbol{\sigma} \cdot \mathbf{n}_0 = \mathbf{0} \qquad \text{on } S_0^{\text{int}} \cup S_0^{\text{ext}} \tag{22}$$

The influence of fixed boundary conditions, $\mathbf{u} \cdot \mathbf{n}_0 = \mathbf{0}$ on $S_0^{\text{int}} \cup S_0^{\text{ext}}$, will be briefly discussed in Sec. 3.3.

3.2. Step 1: computation of the prestress state

Figure 2 shows the local displacement in the x and z directions computed for the prestress state with $p_0 = 20$ bars and $\epsilon_0 = 0.1\%$. As expected, the displacement field exhibits a contracting radial motion of the whole system due to the external pressure (see Fig. 2a), as well as a bending motion of the helical wires due to the tensile load (see Fig. 2b).

Figure 3 shows a zoom inside the contact regions of the mesh updated in its prestress state. Twelve three-node line elements have been used to discretize each contact width, resulting in twenty-five contact nodes and twelve load increments. The convergence of results has been checked by refining the discretization, yielding negligible differences.

As explained later, of special importance for wave propagation are the wire-sheath contact widths. Figure 4 depicts the evolution of both the internal and external contact widths, b_0^{ext} and b_0^{int}, in terms of the normal contact force N_0^{ext} and N_0^{int} respectively, as the prescribed loads are gradually increased up to $p_0 = 20$ bars and $\epsilon_0 = 0.1\%$. For a given contact interface, the normal contact force is obtained as the sum of the contact nodal reactions of the interface projected onto its unit normal (the reaction force vector is given by $\mathbf{R}_0 = \mathbf{K}_0\mathbf{U}_0 - \mathbf{F}_0$).

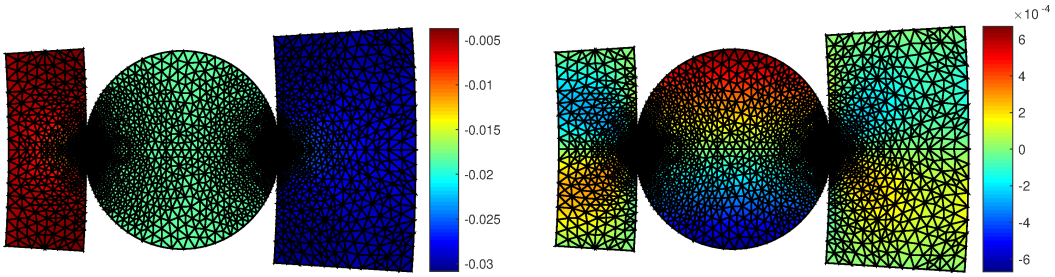

(a) (b)

Figure 2: Local displacement computed for $p_0 = 20$ bars and $\epsilon_0 = 0.1\%$. (a) u_{0_x}/a, (b) u_{0_z}/a (the x-axis is horizontal and the z-axis is out-of-plane).

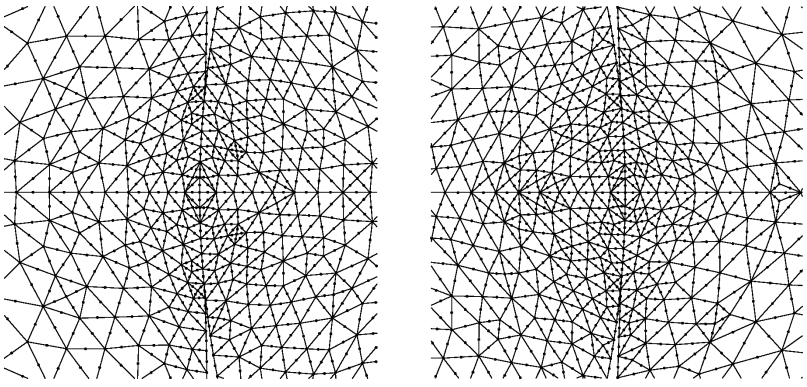

(a) (b)

Figure 3: Zoom of the updated mesh for $p_0 = 20$ bars and $\epsilon_0 = 0.1\%$. (a) Internal contact region, (b) external contact region.

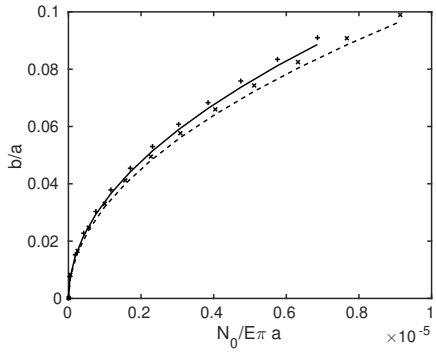

Figure 4: Contact half-width as a function of the contact force. +: numerical results for the external sheath (continuous line: Hertz solution), x: numerical results for the internal sheath (dashed line: Hertz solution).

Also shown in Fig. 4 is the evolution calculated with Hertz theory for parallel cylinders, given by the following analytical solutions [39]:

$$b_0^{\text{ext}} = \sqrt{\frac{4}{\pi} N_0^{\text{ext}} \frac{1}{E^*} \frac{1}{\frac{1}{a} - \frac{1}{R+a}}}, \quad b_0^{\text{int}} = \sqrt{\frac{4}{\pi} N_0^{\text{int}} \frac{1}{E^*} \frac{1}{\frac{1}{a} + \frac{1}{R-a}}} \tag{23}$$

where $\frac{1}{E^*} = \frac{1-\nu^2}{E} + \frac{1-\nu_{\text{PE}}^2}{E_{\text{PE}}}$ (here, ν and E denote the Poisson ratio and Young modulus of steel while ν_{PE} and E_{PE} are those of PE). Note that the external sheath represents a concave contact surface and is hence of negative radius.

The numerical results shown in Fig. 4 are in close agreement with the analytical solution, which validates the static modeling of contact. Since the results are close to those of Hertz theory for parallel cylinders, this also shows that the effect of helical geometry is relatively weak on the contact width in this example (the helix angle and torsion of Table 1 can be considered as small).

One emphasizes that the static state may influence the propagation of guided waves mostly in two ways: by generating prestress inside the structure and by deforming the geometry. The former effect is known to be non-negligible in the very low-frequency regime only (as shown in Ref. [40] for helical beams). This effect is negligible for ultrasonic waves (this has been confirmed by our numerical tests on the armor). On the contrary, the latter effect changes the wire-sheath contact widths and can be non-negligible even in the high-frequency regime, as already found for seven-wire strands [23].

As a side remark, numerical tests have also been performed by varying from 0 to 0.5 the value of the homogenized Poisson's ratio ν_h in the internal static boundary condition given by Eq. (20). It turns out that the contact widths are negligibly influenced by ν_h (results not shown for paper conciseness). Therefore, this parameter is actually of minor importance in our problem.

3.3. Step 2: computation of dispersion curves

The energy velocity dispersion curves of the armor are shown in Fig. 5a for $n = 0$ (*i.e.* rotationally symmetric modes). For comparison, Fig. 5b gives the dispersion curves for a single free wire, that is to say, uncoupled from the sheaths (such a wire follows the same helical pattern as in the armor but is exposed to stress-free boundaries). The L(0,1) fundamental wire mode turns out to be sensitive to the presence of sheaths in the low-frequency range only (this can be observed by sharp changes in Fig. 5a, compared to Fig. 5b). Above a limit frequency Ω_{lim}, roughly equal to 0.5MHz-mm, the numerical results tend to show that the velocity of the L(0,n) modes become weakly affected by the sheaths. Numerical tests with increasing prestress have shown that this limit frequency is weakly influenced by the contact width (results not shown for paper conciseness).

Many low-velocity curves can be observed in Fig. 5a. Such modes mainly resonate inside the PE sheaths (the bulk waves of PE are slow, see Table 2). They are likely to depend on the characteristics of the internal active part and the outer media (marine environment), which are not modeled. These modes are of no interest in the context of this paper. The fact that these low-frequency curves are partially computed in the figure is due to the small number of modes solved at each frequency to reduce the computational time (only 20 modes as mentioned in Sec. 3.1).

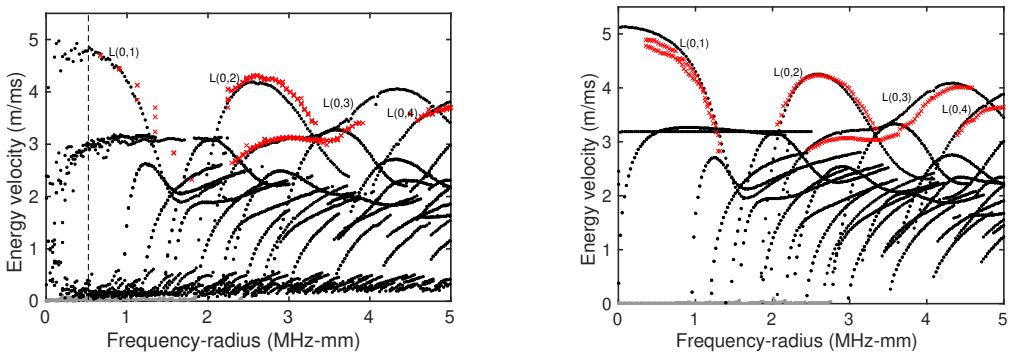

Figure 5: Energy velocity as a function of frequency for: (a) the armor (n=0), (b) a free wire. Red crosses: experimental results. The armor is loaded by $p_0 = 20$ bars and $\epsilon_0 = 0.1\%$. The dashed vertical line indicates the limit frequency Ω_{lim}.

The attenuation dispersion curves of the armor, due to the viscoelastic losses of materials, are given by Fig. 6 for $n = 0$. The normalized attenuation, equal to 8.686Im(ka), is given in dB-mm/m (the natural units of the attenuation Im(k) are Nepers/length, multiplication by 8.686 converts Neper/length to dB/length). Compared to the uncoupled wire (gray curves), modes are more attenuated in the armor. This is an expected result since wires are in contact with the PE sheaths and the viscoelastic loss of PE is much higher than that of steel (see Table 2). As a consequence, the attenuation tends to increase with the contact width. This can be observed in Fig. 6. From Fig. 6a to b and from Fig. 6b to c, the static load has been increased by a factor of 4, yielding an increase of the contact widths by a factor of 2 (according to Eq. (23)).

In the whole frequency range considered, the least attenuated mode is the L(0,1) mode in its low-frequency regime. Below the limit frequency Ω_{lim}, the behavior of this mode is yet dependent on the sheaths and is hence likely to be sensitive to the surrounding media also (this may complicate its use for the NDE of armors).

In the frequency range [2, 4]MHz-mm, the least attenuated modes are the L(0,2) and L(0,3) modes. The velocity of these modes is weakly affected by the sheaths (they occur above Ω_{lim}). Although their attenuation noticeably increases compared to the uncoupled wire, roughly by 50%, these modes could be of interest for the NDE of armors.

Note that the viscoelastic attenuation of the L(0,n) modes is expected to increase as the frequency increases (as found in Ref. [35] for cylindrical bars). In the context of NDE, the longitudinal modes of order 4 and higher are hence probably of less interest.

Figure 7 compares the numerical results computed for the two circumferential orders $n = 0$ and $n = N/2$. Comparing the dispersion curves computed for $n = 0$ with those for $n \neq 0$ actually gives qualitative information about the degree of interwire coupling for each mode (coupling can be considered as weak if a curve tends to remain similar for all n and conversely). The $n = 0$ modes correspond to wires vibrating in phase while the $n = 25$ modes correspond to adjacent wires in opposite phase. The behavior of these two kinds of modes is supposed to be extremely different. However, as observed from a comparison between Fig. 7a and 7b, the differences quickly appear negligible beyond a limit frequency (it has been checked that the dispersion curves for $n = 0$ and $n = 25$, although shown separately in Fig. 7a and 7b in order to quantify the excitability by a color scale, become superimposed). This means that the wires tend to get uncoupled from each other as the frequency increases. This is an expected result because no interwire contact has been assumed. Interestingly, the limit frequency can be quantified thanks to the numerical model. This limit frequency is found to be the same as in Fig. 5a ($\Omega_{\text{lim}} \simeq 0.5$MHz-mm).

Although not shown for paper conciseness, numerical tests have also been performed with fixed boundary conditions $\mathbf{u} \cdot \mathbf{n}_0 = \mathbf{0}$ on $S_0^{\text{int}} \cup S_0^{\text{ext}}$ (instead of free boundary conditions considered in the previous results), yielding negligible difference compared to the results of Fig. 7, except for the L(0,1) mode in its low-frequency region (below the same limit frequency Ω_{lim} as before). This confirms that the higher-order longitudinal modes are expected to be weakly sensitive both to the external medium and to the internal active part of the cable, which has been approximated as a homogenized medium (as previously outlined in Sec. 3.1, the geometry of the internal part usually breaks the helical symmetry of armors and cannot be modeled by the approach proposed in this paper).

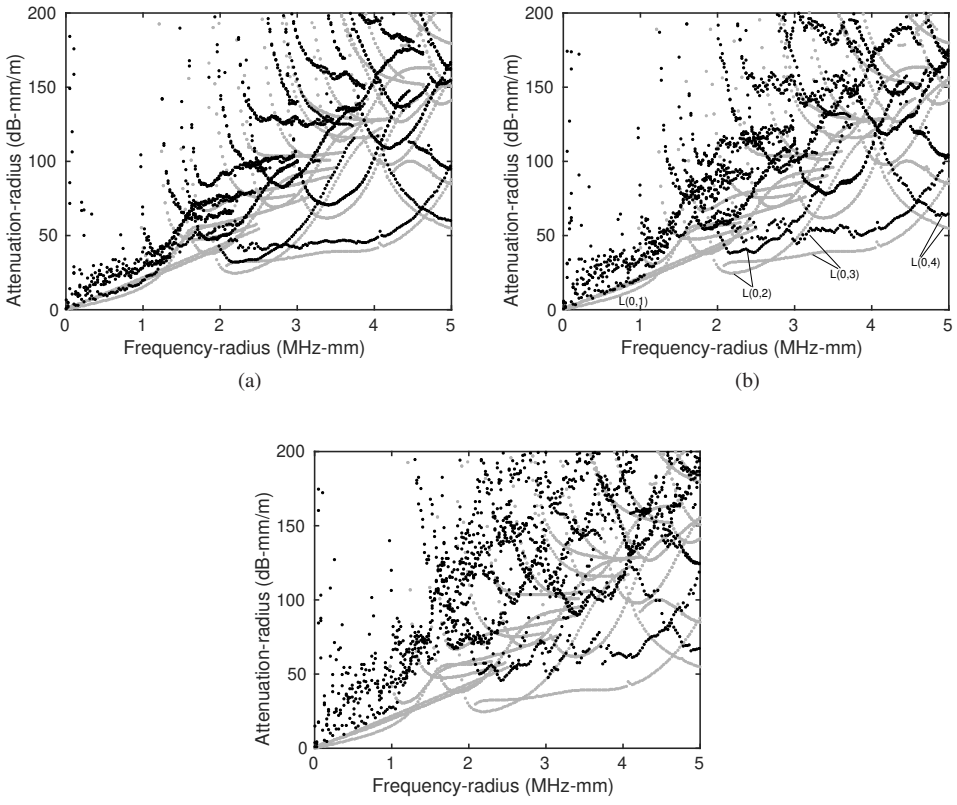

Figure 6: Attenuation as a function of frequency. Black: armor ($n = 0$), gray: free wire. (a) $p_0 = 5$ bars, $\epsilon_0 = 0.025\%$, (b) $p_0 = 20$ bars, $\epsilon_0 = 0.1\%$, (c) $p_0 = 80$ bars, $\epsilon_0 = 0.4\%$.

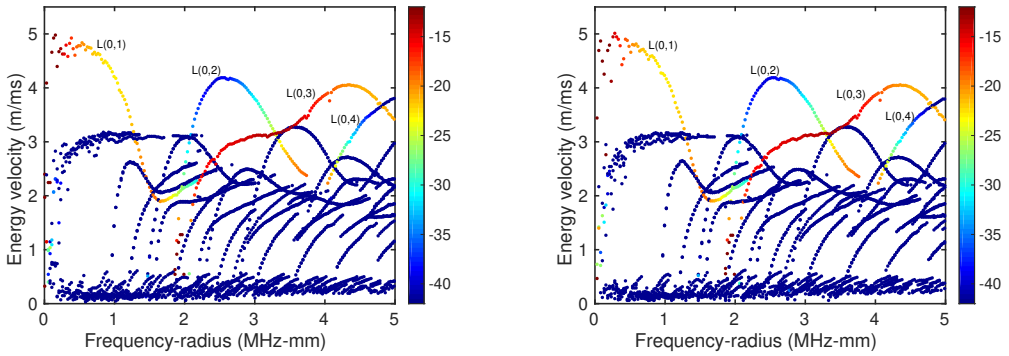

(a) (b)

Figure 7: Energy velocity curves with excitability for the armor: (a) $n = 0$ (b) $n = 25$ ($p_0 = 20$ bars, $\epsilon_0 = 0.1\%$). The color scale corresponds to $20\log_{10}$ of the excitability modulus.

Figure 7 also represents the modal excitabilities, as calculated from Eq. (14), at the wire center and in the z-direction. The point force excitation is also located at the center and oriented in the same direction. As expected for a z-orientation, the most excitable modes are the longitudinal L(0,n) modes. Two remarks can be made. First, the excitabilities of the $n = 0$ and $n = 25$ modes remain nearly identical, which confirms that wires tend to get uncoupled from each other. Second, the most excitable modes are the L(0,1) and the L(0,3) modes. The excitability of the L(0,2) mode is about 25dB lower, which suggests using the L(0,3) rather than the L(0,2) mode in practice.

Also noticeable, the excitability of the L(0,3) mode is the highest in a plateau region, around 3MHz-mm, far below the maximum of its energy velocity (occurring roughly at 4.5MHz-mm, where the excitability is about 10dB lower).

Similarly to the L(0,2) mode, the excitability of the L(0,4) mode is found to be the highest near its cut-off frequency and then decreases with frequency. The fact that the excitability is found to be strong for odd modes (modes 1 and 3) and weak for even modes is consistent with the findings of Refs. [41]. These differences of excitability can be explained from the mode shapes near the wire center (where the point force is applied), significantly lower for even modes than for odd modes.

3.4. Comparison with experiments

Experiments on guided wave propagation have been conducted on a cable sample of length L=75cm. The cable was not intact (not in new condition) but used for real field tests and hence submitted to marine conditions prior to these experiments. Beforehand, the whole sample was cut using a circular saw machine so that both sample cross-section ends are at right angles with the sample longitudinal axis. The cross-section of the sample is shown in Fig. 8. All the measurements have been performed in transmission mode. Two identical 2.25MHz wideband piston-like transducers were used and respectively coupled to each end of a given wire of the armor with a viscoelastic couplant. The arrangement of the transducer attachment is shown in Fig. 9. The ratchet strap and the two plastic pieces insure the active face of each transducer to be at right angle with the cross-section of the probed wire, and a positioning of the transducers easy and stable. Longitudinal modes are predominantly generated and detected in this case. The diameter of the active face of the transducer model used here is slightly larger than the diameter of a constitutive wire (see Fig. 9b). In consequence, the transducer area is in contact with the whole area of the involved wire and with a small part, that is, 1/10 of the area of the two adjacent wires.

In the experiments, tone-burst excitation signals with various center frequency and bandwidths were used. The time excitation signal (a gaussian amplitude-modulated sinusoid) delivered by the function generator (with an input voltage of 1Vpp) fed the transmitting transducer after voltage amplification (typically around 50dB). The measured time signal at the detecting transducer was filtered and amplified (from 40dB up to 80dB) before averaging. As a first example of experimental result, Fig. 10 shows the image of the stacked time signal envelopes of the first wave packet arrival at the receiver (the direct transmitted wave) for a given wire of the cable, obtained by varying the center frequency (here from 2.25 to 4.95MHz-mm) of a narrowband time excitation signal (112.5kHz-mm bandwidth). Between 2.25 and 3.35MHz-mm, the late arrival is the one with the highest amplitude value, and corresponds to the

Figure 8: Picture of the cross-section of the power cable sample used for the experiments.

(a)

(b)

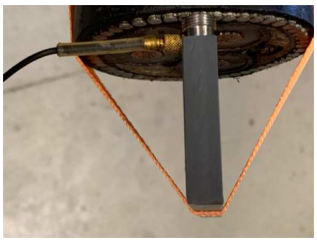

(c)

Figure 9: Pictures of the experimental arrangement for the guided wave transmission measurements for a given wire of the power cable. (a) General view, (b) transducer size versus wire size, (c) local view of the attachment system for the wire cable excitation.

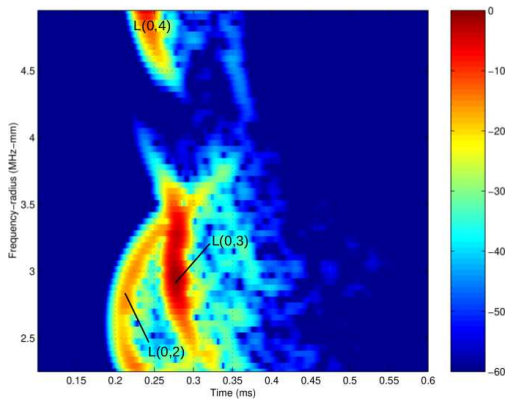

Figure 10: Image of the stacked time signal envelopes of the first wave packet arrival detected in transmission for different excitation signal with centre frequencies varying from 2.25 to 4.95MHz-mm at constant 112.5kHz-mm bandwidth.

L(0,3) mode contribution in its most-excitable frequency region around 3MHz-mm (as discussed and confirmed later by the experimental and simulated group velocity comparison of Fig. 5a as well as the simulated excitability curves of Fig. 7). In the same frequency region, the first arrival corresponds to the L(0,2) mode. Above 4MHz-mm, the time arrival corresponds to the L(0,4) mode and occurs near 5MHz-mm (see Fig. 5a), which is also consistent with the simulation results (around this frequency, both the attenuation and dispersion are rather low and the excitability is not negligible – see Figs. 6 and 7).

Next, the experiments consisted in recording the time history signals over a time-duration, including at least the two first wave packet arrivals (after a $1L$ and a $3L$ propagation distance, respectively), in order to derive the group velocity $v_g(f)$ and the apparent attenuation $\alpha(f)$ from two successive arrivals of the same propagating mode. The extraction of the group velocity are performed by doing a spectrogram time-frequency analysis on the measured signal [5, 42] and picking the mode time arrival as a function of frequency, owing to the following formula:

$$v_g(f) = \frac{t_2(f) - t_1(f)}{2L} \tag{24}$$

where L is the length of the cable sample as mentioned before, t_1 and t_2 are the two successive time arrivals. The apparent attenuation in dB/m is derived from the same spectrogram by picking the amplitude of the mode at the same time arrival (as for the group velocity) as a function of frequency. The apparent attenuation is then extracted as follows:

$$\alpha(f) = -\frac{20}{2L}\log_{10}\left(\frac{A_2(f)}{A_1(f)}\right) \tag{25}$$

where A_1 and A_2 are the two successive amplitudes.

Figure 11 shows an example of spectrogram for another wire (diameter unchanged) of the same cable sample, obtained for a tone burst excitation signal at 2.7MHz-mm (with a 1.125MHz-mm bandwidth). The third time arrival observed at 2.9MHz-mm (occurring roughly at 0.75ms) is relative to the L(0,3) mode, confirming its higher excitability over the L(0,2) mode in this frequency range , as pointed out in the first experiment results (Fig. 10). Additionally, the fundamental L(0,1) mode is also detected in these experiments. Owing to the low attenuation of the L(0,1) mode, three arrivals (corresponding to a propagation distance of $1L$, $3L$ and $5L$ respectively) can be clearly observed near 0.7MHz-mm in the spectrogram, although this mode is excited (and detected) with much less energy by the transducer.

As mentioned before, the identification of modes was allowed by the comparison of the group velocities post-processed from the experiments with numerical results. Figure 5 shows these comparisons both for a wire in the cable (armor configuration) and for the same single wire extracted from the cable (free wire configuration). These preliminary experimental results shown in Fig. 5 confirm the general trends found in the simulations, despite non-negligible discrepancies. In particular, the relatively high-frequency regime of measurements is such that few differences between the cable and the single wire are obtained for the velocity. The differences between the simulations and experiments can be explained by uncertainties related to material properties and further investigation should be

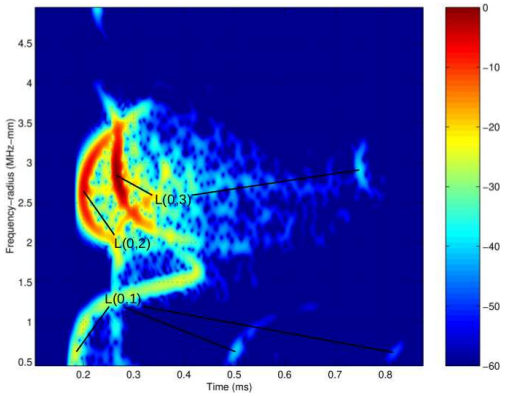

Figure 11: Spectrogram of one time signal detected in transmission for an excitation signal at 2.7MHz-mm with a 1.125MHz-mm bandwidth.

Mode	Frequency (MHz-mm)	Attenuation (dB-mm/m)			
		Wire in the cable		Free wire	
		Experiments	Simulations	Experiments	Simulations
L(0,1)	0.8	[25,34]	18	[7,12]	8
L(0,3)	3	[60,68]	[48,58]	[40,45]	39
L(0,4)	5	[71,87]	69	[63,74]	58

Table 3: Attenuation estimations for longitudinal modes and frequencies at which they have been measured. The simulation results are taken from Fig. 6b (p_0 = 20 bars, ϵ_0 = 0.1%).

addressed in the future on this topic. On the one hand, these properties have been assumed as constant with respect to the frequency in the simulations (they are probably not constant in the experiments). On the other hand, the initial material characteristics of the cable are not intact but have been affected prior to the experiments by real field tests, carried out under marine conditions as already mentioned.

The attenuations of the L(0,1), L(0,3), and L(0,4) modes have been estimated from the experiment data set according to the post data processing explained above. Measurements have been conducted on several wires, first in the cable sample (armor configuration) and then extracted from the armor (free wire configuration). Experimental results are given as intervals owing to the variability of the structural conditions of the wires of the cable sample. In particular, traces of corrosion were more or less visible depending on the wires (only the measurements of healthier wires have been retained here).

The results are shown in Table 3. It can be observed that the lowest frequencies range data exhibit a lower attenuation, confirming the simulation trends. Besides, the relative difference in attenuation between an embedded wire and a single wire gets larger as the frequency range decreases, confirming that the behavior of modes at low frequencies is more affected by the sheaths.

It is noteworthy that the attenuation estimated from these experiments is an apparent attenuation since it involves reflections from the sample ends. End reflection generates conversion into other modes, which possibly lead to an overestimation of the attenuation. This apparent attenuation is also influenced by the presence of a transducer at an end. Even if an estimation of this latter effect has not been yet done by the authors here, a 1dB insertion loss in this frequency range can be reached, according to their experience, which could lead in this case to an overall overestimation of 3dB. Besides the bulk wave attenuations of PE, which have been roughly estimated from the literature, have not been measured and might be different in the real sample. There is also an uncertainty concerning the wire-sheath contact widths, which have been roughly estimated in the experiments as discussed later in Sec. 4.1.

Due to these various uncertainties, the attenuation appears to be slightly underestimated by the simulations. However, it follows the same general trends as in the experiments, which confirms the main conclusions found from the numerical model in Sec. 3.3 concerning the most suitable modes for the NDE of armors. There are actually two

ways to increase the attenuation in the simulations: by increasing the wire-sheath contact widths or by increasing the viscoelastic loss of materials in Table 2. Note that these parameters have not been adjusted in the model to avoid artificial agreement with the experiments (further works would rather be necessary to accurately characterize both the viscoelasticity of materials and the wire-sheath contact of the real cable).

It has to be emphasized that the attenuation of the L(0,2) mode is missing in Table 3. The single-time arrival, found for this mode, does not allow the attenuation to be estimated. This observation is consistent with the numerical results of Fig. 7, predicting a much lower excitability for the L(0,2) mode. Furthermore, it can be observed that the L(0,1) mode in the armor is detected around 0.8MHz-mm, above the limit frequency Ω_{lim} identified from the simulations, and that the L(0,3) mode in the armor is detected around 3MHz-mm, *i.e.* the same frequency as in the simulations. This confirms that the L(0,1) mode can be appropriately propagated, at least from a certain limit frequency, and that the L(0,3) mode is more excitable in a frequency region lower than the frequency of its maximum of group velocity. Note that the numerical result for the L(0,3) mode is also shown as an interval in Table 3 owing to a relatively sharp variation found in the simulations around 3MHz-mm (see Fig. 6b).

4. Discussion about contact

4.1. Quantifying the wire-sheath contact

To estimate the wire-sheath contact pressure of the sample, the outer sheath has been cut and its change in circumference, δ_0, has been measured. Considering the sheath as a cylindrical thin shell, the circumferential prestress can be related to the pressure by: $\sigma_{0_\theta} = p_0 R^{\text{ext}}/h^{\text{ext}}$ where $R^{\text{ext}} = R + a + h^{\text{ext}}$ is the external radius of the sheath. Since $\sigma_{0_\theta} = E_{\text{PE}}\delta_0/2\pi R^{\text{ext}}$, the contact pressure can be estimated from the knowledge of δ_0 as follows:

$$p_0 = \frac{E_{\text{PE}} h^{\text{ext}}}{2\pi (R^{\text{ext}})^2}\delta_0 \tag{26}$$

This yields a value of about 20 bars, which justifies the external pressure prescribed in the numerical model, and hereby, the resulting wire-sheath contact widths. However, such an estimation does not account for the possible plastic deformation of the sheath, which might lead to an underestimation of the circumferential change δ_0 and, hence, of the contact pressure in the model as well as the attenuations predicted in Table 3.

4.2. Neglecting interwire contact

In the model, it has been assumed that there is no contact between adjacent wires. This assumption is probably the most plausible from the visual observation of the sample: as shown in Fig. 8, some adjacent wires appear in contact and others do not. This supports the assumption of a nonexistent contact, or a soft contact, between wires (not sufficient to ensure a significative direct transmission of the acoustic energy).

In addition to this observation, it has to be noted that the ratio R/a itself is such that adjacent wires cannot be in contact. This is clearly visible in Fig. 1b, where the left and right boundaries do not touch the wire circumference. Actually, this absence of interwire contact is a rather widespread design criterion in multi-wire structures for minimizing friction effects (for instance, the peripheral wires of seven-wire strands usually do not touch each other [21]).

In the simulations, the interaction between wires therefore only occurs through the sheaths. Due to the strong impedance mismatch between steel and PE, the behavior of the wires in the armor appears similar to that of a single wire with viscoelastic strip. However, such similarity does no longer hold in a low-frequency regime, where the motion of the structure tends to be of a global type. Figure 12 shows the energy velocity curves in a low-frequency regime: significant differences compared to the free wire, as well as between the n=0 and n=25 modes, are found. These differences are mainly due to velocity drops caused by contact interactions, as already observed in multi-wire cables [23]. These velocity drops correspond to curve veering phenomena, generally found in eigenvalue problems of weakly coupled systems [43, 44], and can be defined as the repulsion of two modal branches, veering away from each other instead of crossing. This shows that each wire cannot be considered independently below a certain frequency. The model proposed in this paper allows to quantify the upper limit frequency of this low-frequency regime, given by $\Omega_{\text{lim}} \simeq 0.5$MHz-mm as previously mentioned in Sec. 3.3.

4.3. Numerical results including interwire contact

For further understanding of propagation mechanisms in armors, it is of interest to evaluate how waves can be affected if contact occurs between adjacent wires. This can be investigated thanks to the numerical model.

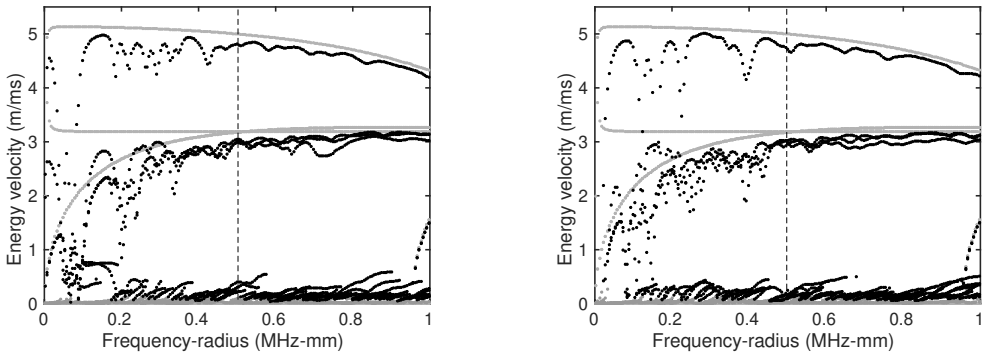

Figure 12: Energy velocity curves for the armor in a low-frequency regime: (a) $n = 0$, (b) $n = 25$ ($p_0 = 20$ bars, $\epsilon_0 = 0.1\%$). Gray curves: free wire. The dashed vertical line indicates the limit frequency Ω_{lim}.

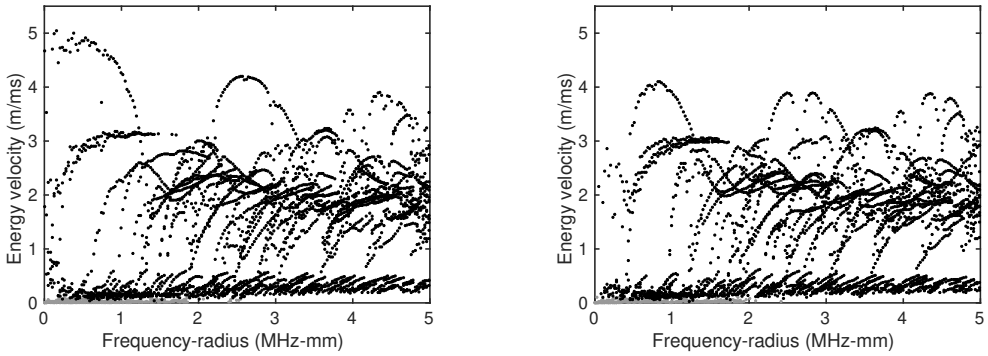

Figure 13: Energy velocity curves for the armor with interwire contact: (a) $n = 0$, (b) $n = 25$.

For simplicity, let us consider an artificial interwire contact point in the cross-section, involving the node pair sketched in Fig. 1b: one node belongs to the left boundary while the other one belongs to the right boundary. The only difference compared to the previous simulations is that these two nodes are hence now linked through the rotational periodic conditions (6).

Figure 13 shows the dispersion curves computed for $n = 0$ and $n = 25$. Large differences are found between these two circumferential orders, indicating significant interwire interactions. Compared to Fig. 7, the longitudinal modes have a quite different dispersive behavior and appear to suffer from strong veering phenomena over the whole frequency range. The simulations including interwire contact are no longer in agreement with the experimental results of Fig. 5. This tends to confirm that the influence of interwire contact on wave propagation has to be neglected, at least for the frequency range and laboratory conditions considered in the experiments.

In real field conditions, it is noteworthy that the contact force between adjacent wires is likely to be greater under high prestress and external pressure (in great depth sea environment). Further experimental works are required to check the possible influence of interwire contact in more realistic conditions, which is out-of-the scope of this paper. More generally, note that the occurrence of interwire contact in armors could also depend on other factors, such as design criteria (R/a ratio) or manufacturing processes (*e.g.* thermal stress).

5. Conclusion

A numerical method has been proposed to investigate the propagation of guided waves in helical multi-wire armors. The method combines a SAFE method written in twisting coordinates, to account for the continuous screw symmetry of the problem, with Bloch conditions of rotational type in the cross-section in order to account for the high order of the discrete rotational symmetry. The existence of wave modes along the two directions (screw axis and circumferential direction) has been justified from a theoretical point of view thanks to the calculation of the metric tensor in a mixed twisting-polar coordinate system. The formulation hence allows the initial three-dimensional problem to be reduced to a two-dimensional unit cell involving only one wire. Numerical results have been presented for a typical armor of power cable. The analysis has focused on longitudinal wave modes propagating predominantly inside the wires. A comparison with experimental measurements has been carried out. The results show that the modal velocity of longitudinal waves behaves as in a single free wire above a limit frequency, quantified by the model, so that in practice, the velocity of the L(0,n) wire modes ($n \geq 2$) is nearly unaffected by the armor. This is not the case of their attenuation, always greater in the armor due to mechanical contact with the viscoelastic sheaths. The least attenuated mode is the L(0,1) mode. This mode is in a low-frequency regime where waves are likely to be sensitive to the internal part and to the external media surrounding the armor. Although more attenuated, the L(0,3) appears to be weakly affected by the sheaths. This mode is also highly excitable, in a plateau region occurring below the maximum of its energy velocity. The influence of mechanical contacts, in particular interwire contact, has also been discussed. With interwire contact, the velocity behavior of longitudinal modes is destroyed by curve veering phenomena, which contradicts the experimental observations (in laboratory conditions). Using appropriate excitation frequencies, both the L(0,1) and L(0,3) modes could be of potential interest for the NDE of armors. The present paper paves the way for further experimental studies to evaluate the influence of sea environmental conditions and the sensitivity of guided waves to defects in armors of power cables. Furthermore, the numerical approach could be applied to investigate wave propagation in the armors of flexible pipes, the wires of which are usually not circular but flat (rectangular cross-section).

Acknowledgements

This work was carried out within the framework of the WEAMEC West Atlantic Marine Energy Community, and with funding from the Pays de la Loire Region (France). The authors would like to thank the two anonymous reviewers for their careful reading of the manuscript, suggestions and comments.

References

[1] P. D. Wilcox, M. J. S. Lowe, P. Cawley, Mode and transducer selection for long range Lamb wave inspection, Journal of Intelligent Material Systems and Structures 12 (2001) 553–565.

[2] H.-C. Chang, B.-F. Chen, Mechanical behavior of submarine cable under coupled tension, torsion and compressive loads, Ocean Engineering 189 (2019) 106272.

[3] M. A. Vaz, N. A. S. Rizzo, A finite element model for flexible pipe armor wire instability, Marine Structures 24 (2011) 275–291.

[4] H. Kwun, K. A. Bartels, J. J. Hanley, Effects of tensile loading on the properties of elastic-wave propagation in a strand, Journal of the Acoustical Society of America 103 (1998) 3370–3375.

[5] L. Laguerre, J. C. Aime, M. Brissaud, Magnetostrictive pulse-echo device for non-destructive evaluation of cylindrical steel materials using longitudinal guided waves, Ultrasonics 39 (2002) 503–514.

[6] P. Rizzo, F. L. di Scalea, Wave propagation in multi-wire strands by wavelet-based laser ultrasound, Experimental Mechanics 44 (2004) 407–415.

[7] S. Chaki, G. Bourse, Guided ultrasonic waves for non-destructive monitoring of the stress levels in prestressed steel strands, Ultrasonics 49 (2009) 162–171.

[8] I. Bartoli, S. Salamone, R. Phillips, F. Lanza di Scalea, C. S. Sikorsky, Use of interwire ultrasonic leakage to quantify loss of prestress in multiwire tendons, Journal of Engineering Mechanics 137 (2011) 324–333.

[9] C. Nucera, F. Lanza di Scalea, Monitoring load levels in multi-wire strands by nonlinear ultrasonic waves, Structural Health Monitoring 10 (2011) 617–629.

[10] A. Farhidzadeh, S. Salamone, Reference-free corrosion damage diagnosis in steel strands using guided ultrasonic waves, Ultrasonics 57 (2015) 198–208.

[11] C. Schaal, S. Bischoff, L. Gaul, Energy-based models for guided ultrasonic wave propagation in multi-wire cables, International Journal of Solids and Structures 64-65 (2015) 22–29.

[12] B. Dubuc, A. Ebrahimkhanlou, S. Salamone, Higher order longitudinal guided wave modes in axially stressed seven-wire strands, Ultrasonics 84 (2018) 382–391.

[13] J. Qian, X. Chen, L. Sun, G. Yao, X. Wang, Numerical and experimental identification of seven-wire strand tensions using scale energy entropy spectra of ultrasonic guided waves, Shock and Vibration 2018 (2018) 1–11.
[14] A. Baltazar, C. D. Hernandez-Salazar, B. Manzanares-Martinez, Study of wave propagation in a multiwire cable to determine structural damage, NDT and E International 43 (2010) 726–732.
[15] M. Legg, M. K. Yücel, V. Kappatos, C. Selcuk, T.-H. Gan, Increased range of ultrasonic guided wave testing of overhead transmission line cables using dispersion compensation, Ultrasonics 62 (2014) 35–45.
[16] M. K. Yücel, M. Legg, V. Kappatos, T.-H. Gan, An ultrasonic guided wave approach for the inspection of overhead transmission line cables, Applied Acoustics 122 (2017) 23–34.
[17] P. Zhang, Z. Tang, F. Lv, K. Yang, Numerical and experimental investigation of guided wave propagation in a multi-wire cable pengfei, Applied Sciences 9 (2019) 1–18.
[18] R. Raišutis, R. Kažys, L. Mažeika, E. Žukauskas, V. Samaitis, A. Jankauskas, Ultrasonic guided wave-based testing technique for inspection of multi-wire rope structures, NDT and E International 62 (2014) 40–49.
[19] R. Raišutis, R. Kažys, L. Mažeika, V. Samaitis, E. Žukauskas, Propagation of ultrasonic guided waves in composite multi-wire ropes, Materials 9 (2016) 451.
[20] F. Treyssède, L. Laguerre, Investigation of elastic modes propagating in multi-wire helical waveguides, Journal of Sound and Vibration 329 (2010) 1702–1716.
[21] A. Frikha, P. Cartraud, F. Treyssède, Mechanical modeling of helical structures accounting for translational invariance. part 1: Static behavior, International Journal of Solids and Structure 50 (2013) 1373–1382.
[22] F. Treyssède, A. Frikha, P. Cartraud, Mechanical modeling of helical structures accounting for translational invariance. part 2: Guided wave propagation under axial loads, International Journal of Solids and Structure 50 (2013) 1383–1393.
[23] F. Treyssède, Dispersion curve veering of longitudinal guided waves propagating inside prestressed seven-wire strands, Journal of Sound and Vibration 367 (2016) 56–68.
[24] T. Hayashi, W.-J. Song, J. L. Rose, Guided wave dispersion curves for a bar with an arbitrary cross-section, a rod and rail example, Ultrasonics 41 (2003) 175–183.
[25] I. Bartoli, A. Marzani, F. Lanza di Scalea, E. Viola, Modeling wave propagation in damped waveguides of arbitrary cross-section, Journal of Sound and Vibration 295 (2006) 685–707.
[26] H. Gravenkamp, H. Man, C. Song, J. Prager, The computation of dispersion relations for three-dimensional elastic waveguides using the scaled boundary finite element method, J. Sound Vib. 332 (2013) 3756–3771.
[27] L. Gry, C. Gontier, Dynamic modelling of railway track : A periodic model base on a generalized beam formulation, Journal of Sound and Vibration 199 (1997) 531–558.
[28] B. R. Mace, D. Duhamel, M. J. Brennan, L. Hinke, Finite element prediction of wave motion in structural waveguides, The Journal of the Acoustical Society of America 117 (2005) 2835–2843.
[29] F. Treyssède, Free and forced response of three-dimensional waveguides with rotationally symmetric cross-sections, Wave Motion 87 (2019) 75–91.
[30] K. J. Bathe, Finite Element Procedures, Prentice Hall, Englewood Cliffs, New Jersey, 1996.
[31] P. Wriggers, Computational Contact Mechanics, Springer-Verlag, Berlin, 518 p.
[32] D. J. Mead, A general theory of harmonic wave propagation in linear periodic systems with multiple coupling, Journal of Sound and Vibration 27 (1973) 235–260.
[33] R. S. Langley, A variational principle for periodic structures, Journal of Sound and Vibration 135 (1989) 135–142.
[34] F. Treyssède, Mode propagation in curved waveguides and scattering by inhomogeneities: application to the elastodynamics of helical structures, Journal of the Acoustical Society of America 129 (2011) 1857–1868.
[35] B. N. Pavlakovic, M. J. S. Lowe, P. Cawley, High-frequency low-loss ultrasonic modes in embedded bars, Journal of Applied Mechanics 68 (2001) 67–75.
[36] J. S. Egerton, M. J. S. Lowe, P. Huthwaite, H. V. Halai, Ultrasonic attenuation and phase velocity of high-density polyethylene pipe material, Journal of the Acoustical Society of America 141 (2017) 1535–1545.
[37] C. Geuzaine, J.-F. Remacle, Gmsh: a three-dimensional finite element mesh generator with built-in pre- and post-processing facilities, International Journal for Numerical Methods in Engineering 79 (11) (2009) 1309–1331.
[38] R. Lehoucq, D. Sorensen, C. Yang, ARPACK User's Guide: Solution of Large Scale Eigenvalue Problems with Implicitly Restarted Arnoldi Methods, SIAM, Philadelphia, PA, 1998.
[39] K. L. Johnson, Contact Mechanics, University Press, Cambridge, 1985.
[40] A. Frikha, F. Treyssède, P. Cartraud, Effect of axial load on the propagation of elastic waves in helical beams, Wave Motion 48 (2011) 83–92.
[41] M. Gallezot, F. Treyssde, L. Laguerre, A modal approach based on perfectly matched layers for the forced response of elastic open waveguides, J. Comp. Phys. 356 (2018) 39–409.
[42] L. Laguerre, F. Treyssède, Non destructive evaluation of seven-wire strands using ultrasonic guided waves, European Journal of Environmental and Civil Engineering 15 (2011) 487–500.
[43] N. C. Perkins, C. D. Mote, Comments on curve veering in eigenvalue problems, Journal of Sound and Vibration 106 (1986) 451–463.
[44] C. Pierre, Mode localization and eigenvalue loci veering in disordered structures, Journal of Sound and Vibration 126 (1988) 485–502.